



# The role of incoherent twin boundaries on the plasticity of Cu micropillars

Reza Hosseinabadi<sup>a</sup>, Andrea Brognara<sup>a</sup>, Christoph Kirchlechner<sup>a,b</sup>, James P. Best<sup>a,\*</sup>,  
Gerhard Dehm<sup>a,\*</sup>

<sup>a</sup> Max-Planck-Institut für Eisenforschung GmbH, Germany

<sup>b</sup> Institute for Applied Materials, Karlsruhe Institute of Technology, Germany

## ARTICLE INFO

### Keywords:

Dislocation  
Incoherent twin boundary  
Thin film  
Compression  
Micropillars

## ABSTRACT

The role of a  $\Sigma 3\{112\}$  incoherent twin boundary (ITB) on the shear stress of Cu at the micron scale has been investigated through microcompression of bi-crystalline pillars containing ITB, as well as single-crystalline pillars, in two different compression directions. The Cu sample containing ITBs was synthesized using magnetron sputtering on a sapphire substrate. Firstly, pillars along  $[111]$  compression direction were milled on the film surface. As multiple slip systems were activated upon loading, the dislocation-ITB interaction in this direction was dominated by the dislocation-dislocation interactions. Another set of pillars was milled from the side of the film (in the thickness of the film) in a nominally  $[13\bar{4}]$  compression direction. Compression in this direction activated a single slip in each grain, which facilitated the investigation of the interaction between dislocations and ITBs. *Post-mortem* images showed that slip traces were not distinctly connected at the boundary unlike ideal slip transmission in pillars containing a coherent twin boundary. Moreover, bi-crystalline pillars in the single slip direction are stronger than single-crystalline pillars. The observations indicate that ITBs are not impenetrable for dislocations, but the boundary demonstrates some resistance to transmission.

## 1. Introduction

Grain boundaries (GBs) are known to affect the mechanical behavior of metals remarkably. They influence plastic properties such as yield strength and work hardening, as well as damage nucleation, crack propagation and fracture toughness of materials [1–3]. Besides, the deformation of face centered cubic (FCC) materials is usually achieved by dislocation slip or twinning [4]. Therefore, studying the interactions of dislocations with GBs is pivotal in understanding the mechanical behavior of FCC metals. Among various GBs, twins are of great importance in FCC metals due to their abundance, as a result of low formation energy [5–7]. Moreover, the introduction of nanotwins to the material is reported to cause exceptional properties like coincident ultrahigh strength and ductility [8–11]. In order to gain a comprehensive understanding of GB behavior in complex stress states of polycrystalline materials, it is imperative to investigate the behavior of individual GBs as fundamental building blocks.

To decipher the role of individual twins in materials' mechanical properties, numerous experimental [12–18] and simulation [19–21] studies focused on the interaction of dislocations with  $\Sigma 3\{111\}$  coherent twin boundaries (CTB). However, not all twins extend across

the entire grain, and those twins terminating inside a grain possess, in addition to the  $\Sigma 3\{111\}$  coherent sections, also an incoherent twin boundary (ITB), for instance  $\Sigma 3\{112\}$  [22]. Unlike CTBs, the nearest neighbor coordination is changed around the ITB, therefore they are associated with much higher GB energy. Schmidt et al. calculated the CTB energy to be  $19.9 \text{ mJm}^{-2}$  in Cu [23], while it is estimated to be  $540 \text{ mJm}^{-2}$  for the  $\Sigma 3\{112\}$  ITB [24]. A similar ratio for CTB and ITB is also obtained in the case of Ni, where the CTB GB energy is  $64 \text{ mJm}^{-2}$  and  $879 \text{ mJm}^{-2}$  for the  $\Sigma 3\{112\}$  ITB [25]. It is noteworthy that the boundary plane of ITB is not limited to  $\{112\}$ , and other GB planes are also reported to exist. For copper, such ITB can have even slightly lower energy cusps than  $\Sigma 3\{112\}$  [24], but only  $\Sigma 3\{112\}$  and  $\Sigma 3\{110\}$  form symmetrical boundaries.

In thin films, the incoherent sections can be even more abundant than the coherent sections due to the geometrical factors, elastic properties and surface energies, which facilitate the growth of specific grain orientations. For instance, in metal films grown on single crystalline sapphire ( $\alpha\text{-Al}_2\text{O}_3$ ), the hexagonal symmetry of the (0001) plane translates into the defined orientation of the film's microstructure [26]. Based on this orientation relationship, the existence of ample incoherent  $\Sigma 3\{112\}$  growth twins has been reported in the epitaxial growth of Al

\* Corresponding authors.

E-mail addresses: [j.best@mpie.de](mailto:j.best@mpie.de) (J.P. Best), [dehm@mpie.de](mailto:dehm@mpie.de) (G. Dehm).

<https://doi.org/10.1016/j.matdes.2023.112164>

Received 31 March 2023; Received in revised form 20 June 2023; Accepted 11 July 2023

Available online 14 July 2023

0264-1275/© 2023 The Authors. Published by Elsevier Ltd. This is an open access article under the CC BY license (<http://creativecommons.org/licenses/by/4.0/>).

on a (0001)  $\alpha$ -Al<sub>2</sub>O<sub>3</sub> sapphire substrate [27,28]. Depending on the deposition conditions, orientation relation one (OR I)  $\{111\} \pm \langle 0\bar{1}1 \rangle \text{ Cu} \parallel \{0001\} \langle 10\bar{1}0 \rangle \alpha\text{-Al}_2\text{O}_3$  or orientation relation two (OR II)  $\{111\} \pm \langle 0\bar{1}1 \rangle \text{ Cu} \parallel \{0001\} \langle 2\bar{1}\bar{1}0 \rangle \alpha\text{-Al}_2\text{O}_3$  could be achieved [29]. The  $\pm$  sign in the OR indicates the two grain variants separated by an ITB. Epitaxial growth of other FCC metal films such as Al [27,28,30], Ni [31], Cu [26,29] and even CoCrFeNi films [32] on (0001)  $\alpha$ -Al<sub>2</sub>O<sub>3</sub> sapphire substrate has been reported to have similar maze-like structures, with surface normal of  $\langle 111 \rangle$  and two types of growth orientation relationships and their twins.

TEM studies of the  $\Sigma 3\{112\}$  GB showed that the ITB consists of periodically repeated Shockley partial dislocations on each of three  $\{111\}$  planes making the ABC stacking sequence [33,34]. Wang et al. [35] reported the migration of ITBs under shear stress in the growth twins. The migration led to detwinning and showed the unstable nature of ITBs, caused by the glide of Shockley partials of the boundary. Using *in situ* nanoindentation in TEM, Li et al. [36] reported the ITB migration in a Cu film by propagation of steps or disconnections, as a result of dislocation-ITB interaction. Molecular dynamics (MD) simulations of the dislocation transmission across  $\Sigma 3\{112\}$  indicate that transmission of a mixed dislocation takes place, when the leading partial and pre-existing partial at the ITB form a full dislocation. Otherwise, the incoming dislocation is blocked by the ITB [37]. Ma et al. [38], using MD and phase field studies on the transmission of dislocations at ITB revealed that not all transmissions are direct. The transmission behavior and the shear stress needed for that depends on which of the three repeating planes the gliding dislocation is impacting [33].

Experimental studies aimed at a mechanistic understanding of the dislocation structure at an ITB [33], movement of dislocations on an ITB [34] and dislocation transmission across an ITB and its impact on boundary migration [36] were performed in TEM. Since these samples for TEM must be electron transparent, very high stresses are present that move dislocations through the thin foil. Consequently, potential mechanisms that require lower stresses in larger samples (i.e. micron scale or bulk) could be masked. An important tool to study the mechanics of materials at the micron scale is micropillar compression, which was first introduced by Uchic et al. [39]. To the best of our knowledge, no research has yet focused on the ITB strength contribution and the dislocation transmission behavior through ITBs in micron-sized samples. Such experiments are challenging due to the high energy of ITBs, as well as sample requirements for a successful micro-compression study. The flow stress in micron-sized samples has a stochastic behavior as a result of the availability of dislocation sources [9,40]. Therefore, a quantitative conclusion based on micro-compression testing often requires a high number of measurements of samples for statistical reasons, as previously reported by our group for pillars containing a CTB [12,15].

In this paper, we employed physical vapor deposition (PVD) to synthesize a 6  $\mu\text{m}$  thick Cu film on single crystalline (0001) sapphire with two twin related grain variants for OR I, which consist mainly of ITBs. Micron-sized pillars containing ITBs, as well as single-crystalline pillars in two different nominal sizes were milled and tested on the Cu film. A new milling configuration from the side of the film was proposed to avoid compression along the  $[111]$  direction and associated multiple slip activation, which may obscure the dislocation-grain boundary interaction by dislocation-dislocation interactions. The transmission behavior of dislocation through ITBs and the strength contribution of the ITB based on two different pillar orientations are reported and critically discussed.

## 2. Experimental details and data analysis

### 2.1. Thin film deposition

The sample required for the micropillar compression containing ITB

was synthesized using PVD film deposition. The Cu film was deposited by a magnetron sputtering apparatus (Bestec GmbH), using 99.999% pure Cu targets mounted on both RF and DC cathodes. Prior to deposition, the chamber was pumped down to a base vacuum pressure  $< 10^{-6}$  Pa, after which Ar gas was introduced at a rate of 20  $\text{cm}^3/\text{min}$  to reach a pressure of 0.5 Pa. The substrate was placed at a distance of 239 mm from the cathodes and rotated at 30 rpm to obtain thickness homogeneity across the 2-inch (0001) oriented  $\alpha$ -Al<sub>2</sub>O<sub>3</sub> substrate. The deposition process was divided into two steps: i) Firstly, an initial 500 nm thick Cu layer was grown at  $T_{\text{room}}$  on top of a single crystal (0001) sapphire ( $\alpha$ -Al<sub>2</sub>O<sub>3</sub>) substrate, using an RF cathode with an applied power of 250 W and subsequently annealed at 320 °C for 2 h inside the deposition chamber. This was done to facilitate the growth of the desired  $[111]$  grains in the next step, similar to the method reported in a previous work from our group [41]. ii) In the second step, the deposition continued for 2 h 45 min employing co-sputtering with RF and DC cathodes both at 250 W at 320 °C to increase the deposition rate. A total film thickness of  $\sim 6 \mu\text{m}$  was achieved. Finally, the film was annealed at 320 °C for 45 min to promote grain growth. The film microstructure, including the grain size will be reported in section 3.1.

### 2.2. Pillar milling in two directions

Using annular Ga focused ion beam (FIB) milling at 30 kV, two sets of pillars were produced with differing compression directions. The first set of pillars was milled on the film surface, with a compression direction oriented along  $[111]$ . This is shown schematically in Fig. 1a. The  $[111]$  micropillars were fabricated at 2 nominal diameter sizes of 1.5 and 3  $\mu\text{m}$ . In total, 46 cylindrical pillars were milled in this direction, 18 of which contained a boundary (Bxx) and 12 were single-crystalline (Sxx). After deformation, 16 of the pillars were excluded based on SEM inspection, as it was unclear from the slip traces whether they contained a vertical boundary, or the boundary was straight from the surface to the substrate.

The  $[111]$  pillars had six slip systems with the highest Schmid factor, which were activated in compression. In order to focus on the dislocation-ITB interaction, a different compression direction was required to facilitate single slip in each crystal. To achieve this in the copper film, the second set of pillars was milled into the side of the film, parallel to the film/substrate interface, as shown schematically in Fig. 1b. As pillars need to have a single slip compression direction, the film should be first cut in a specific direction. Sapphire tends to fracture on preferred cleavage planes, either  $\{11\bar{2}0\}$  or  $\{10\bar{1}0\}$  [42]. This causes the Cu film to break along planes of the  $\{110\}$  family, which again promotes multi-slip. An attempt to cut the film in a pre-selected direction was made using a diamond saw. Nonetheless, this method proved ineffective, as the indenter tip could not approach the pillars without touching the hard sapphire. This method is discussed in details in S2 section in the supplementary document.

Ultimately, a part of the film that was freestanding at the edge of the film/substrate was employed for pillar milling. A diamond pen was used to scratch the film from the top side, and then the two pieces were detached using tweezers. Because the Cu film with this thickness was ductile, the film deformed in the fracture area. This caused a small part of the film to be freestanding (approximately 50  $\mu\text{m}$ ). Next, this freestanding portion of the film was FIB cut until only a few micrometres of freestanding film material extended from the substrate (blue arrows in Fig. 1b). The final step of removal was done with a low current (240 pA) to obtain a smooth surface, as this would serve as the top contact surface of the pillars in the next step. The in-plane direction of the film in the cut region is  $\sim 5^\circ$  different in the two grains, and is nominally along  $[13\bar{4}]$ . Then the sample is rotated inside the microscope chamber, so that the FIB beam was parallel to the  $[13\bar{4}]$  direction and the pillars were milled into the thickness of the Cu film (see Fig. 1b). The  $[13\bar{4}]$  pillars were milled with a diameter of 2.2  $\mu\text{m}$ . In total 5 annular pillars were milled

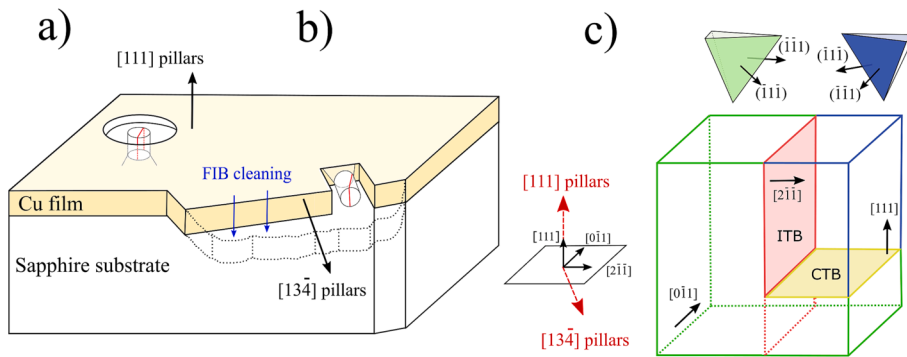


**Fig. 1.** Schematic configuration of the Cu film on the substrate and two sets of pillars. a) Pillar compression along [111] direction, b) pillars compressed along [134] through the thickness of the film. Pillars are milled at a freestanding part of the film with a compression direction that promotes a single slip. Prior to milling the pillars, FIB was used to remove large portions of the freestanding film to reach a smooth surface (blue arrows). c) Schematic of two grains and their corresponding Thompson tetrahedron. The  $\Sigma 3\{2\bar{1}1\}$  ITB between them is shown which separates the two grains. CTB  $\Sigma 3\{111\}$  plane is also shown for comparison. The compression direction for [111] and at [134] pillars are marked with red arrows. (For interpretation of the references to colour in this figure legend, the reader is referred to the web version of this article.)

and tested successfully, out of which 2 were Bxx.

Fig. 1c shows the twin grains with their Thompson tetrahedra. There is a  $60^\circ$  misorientation between the blue and green grain (corresponding to  $\Sigma 3$ ). The boundary plane between the grains is decisive whether the twin is an ITB or CTB. If the GB plane between the grains has a normal of  $\{112\}$  type, the GB is ITB (red plane). In case of a CTB, the boundary is of  $\{111\}$  type, one of which is shown as the green plane to compare with ITB. The two compression directions are marked with red arrows in the legend. For [111] pillars, the compression direction is the same for both grains, and the ITB lies parallel to the compression axis. Whereas for [134] case, the boundary is nonparallel to compression axis. This results in a different compression direction in two grains. Moreover, the grain boundary plane does not run straight from surface to the base of pillar, as schematically shown in Fig. 1b.

All cylindrical micropillars were cut using a Zeiss Auriga® FIB workstation in two milling steps using currents ranging from 2 nA to 240 pA. The cleaning step for removing the parts of the film (blue arrows in Fig. 1b) was done using 16 nA currents, and the final polishing with 240 pA. The aspect ratio of diameter to the length was kept between 2 and 3 to avoid buckling. The pillars were milled either within one of the single crystalline (Sxx) regions or at the incoherent boundary (Bxx). However, the incoherent twin boundary was in most cases not straight and usually deviated from the original plane below the surface.

### 2.3. Mechanical testing and analysis

Compression of all pillars was performed using a Bruker Hysitron P188 indenter with a flat diamond punch of  $5\ \mu\text{m}$  (for  $3\ \mu\text{m}$  pillars) and  $3\ \mu\text{m}$  for all other pillars (Synton-MDP, Switzerland). All tests were performed in displacement-controlled mode at a nominal strain rate of  $10^{-3}\ \text{s}^{-1}$ . Each pillar was unloaded to zero at about every 5% of strain to reduce instrumental constraints [14,43,44]. Compression tests were done *in situ* inside the Zeiss Gemini 500® scanning electron microscopy (SEM), and were followed by *post-mortem* imaging using an in-lens detector and electron backscatter diffraction (EBSD). Some of the *post-mortem* micrographs were sharpened using Adobe Photoshop for better detection of slip traces.

Each pillar diameter was measured both at the top and bottom cross-section before compression. An average of the top and bottom values was used to calculate the engineering stress. A Mathematica® script was then used to determine the stress–strain curves from the force–displacement raw data from the indenter. The stress at 2% strain was chosen to compare different pillars to minimize the impact of dislocation–dislocation interactions.

## 3. Results and interpretation

This chapter begins with the characterization of the deposited Cu

film on sapphire. Section 3.2 reports the results for the [111] compression direction of micropillars containing an ITB. Finally, section 3.3 describes the micro-compression test results of the ITB containing pillars in [134] single slip compression direction.

### 3.1. Characterization of Cu film on sapphire

The sample was synthesized by employing magnetron sputtering to deposit a  $6\ \mu\text{m}$  thick Cu film on the sapphire substrate, which has sufficient thickness for performing micro-compression tests. The majority of the grains have an average diameter larger than  $10\ \mu\text{m}$ , permitting micrometer sized pillars to be milled in the film. Fig. 2a shows a trench that was milled using FIB to observe the cross-section of the film. The red arrow marks the  $500\ \text{nm}$  thin layer grown in the first step of deposition using the RF cathode. This layer has much smaller grains ( $\sim 0.5\ \mu\text{m}$ ) compared to the grains in the second, much thicker layer. There is a visible interface between the two layers. Fig. 2b shows the inverse pole figure map from EBSD of the surface of the film, where it can be observed that all grains have a [111] surface normal. The presence of only two distinct,  $60^\circ$  twin-related grain orientations in OR I was intended to facilitate ITB growth between them, as shown in Fig. 2d. The GB between these grains has a coincidence site lattice (CSL) of  $\Sigma 3$  and has an incoherent nature due to the film normal direction being [111]. Although the GB plane is not the same everywhere, the most dominant GB plane observed on the film surface is  $\{112\}$ .

The cross section of the film in Fig. 2a shows that the GBs do not always run straight from the surface to the substrate. Still, some boundary segments are mostly straight (see yellow arrow in Fig. 2a). The significant energy difference between ITB and CTB gives rise to the evolution of CTBs facets along the ITB, resulting in a curved GB appearance. Besides short facets, extended excursions of CTB may be also found in the film due to their low formation energy. Moreover, there are some GBs buried in the film, like the white arrow in Fig. 2a. Therefore, whether a pillar is single crystalline, bi-crystalline or even contains buried boundaries can be determined only after *post-mortem* analysis.

### 3.2. Compression of pillars containing an ITB in [111] direction

The first set of pillars was milled using FIB perpendicular to the film surface, so that the compression direction of both grains was [111] (see Fig. 1a). The Bxx pillars were placed where a  $\Sigma 3\{112\}$  ITB was identified at the sample surface. However, as shown in Fig. 2a, the boundary might deviate through the pillar's height. Therefore, whether pillars are Sxx or Bxx could only be confirmed by slicing the pillar after compression testing.

*Pre- and post-mortem* SEM images of 3 representative Bxx pillars are summarized in Fig. 3. There are multiple slip systems with the highest

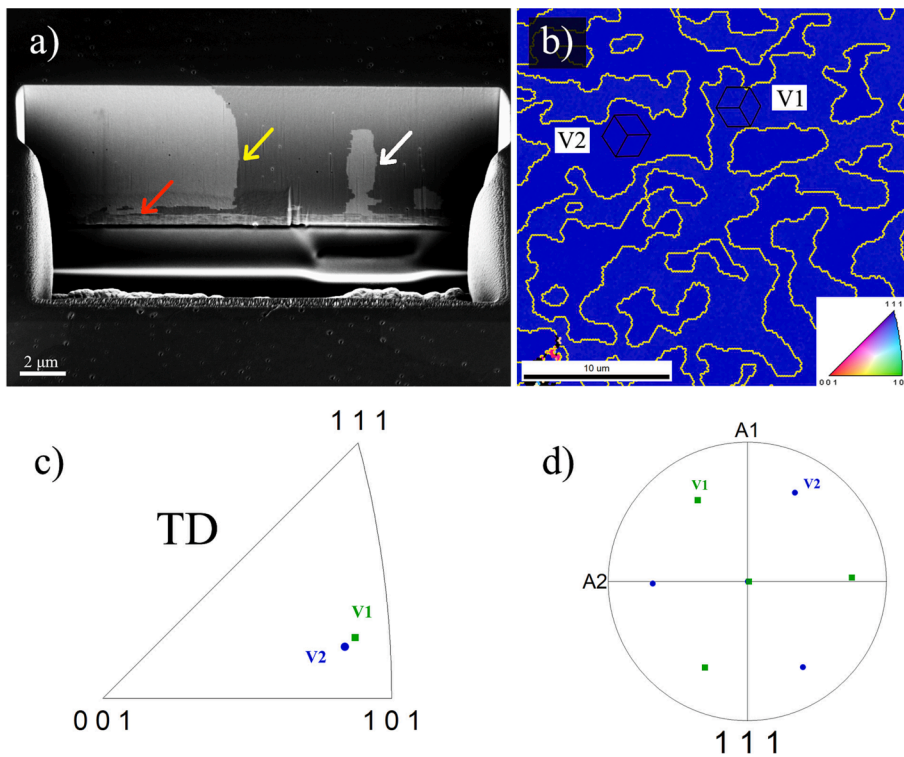


**Fig. 2.** a) A trench cut in the Cu film using FIB, shows the cross-section of the deposited film on a (0001) oriented sapphire substrate. Two types of GB can be identified, which according to EBSD are ITB (perpendicular to the surface of the film) and CTB (horizontal). Curved segments consist of alternating CTB and ITB facets, while some micron-sized sections are straight ITB (see yellow arrow). Long CTB segments (near red arrow) or even buried grains (white arrow) can be also found in the film. b) Inverse pole figure map from the surface of the Cu film reveals two twin-related grain orientations having both a [111] normal direction. c) Inverse pole figure showing slight angular deviation of the two orientations in the transverse direction. d) {111} pole figure of the film surface. The two-grain variations with 60° misorientation are visible. (For interpretation of the references to colour in this figure legend, the reader is referred to the web version of this article.)

Schmid factor activated in each grain (see Fig. 3g). Note that the (111) plane, which continues across the ITB and thus permits easy transmission, has a critical resolved shear stress of zero. Thus, transmission must occur on the other three planes of the Thompson tetrahedron, namely  $(\bar{1}11)$ ,  $(\bar{1}\bar{1}1)$  and  $(\bar{1}1\bar{1})$ , which all have similar Schmid factors. Therefore, slip traces for both cases of  $S_{xx}$  (shown in Fig. S1 in the supplementary document) and  $B_{xx}$  are faint and distributed across the entire height of the pillar. For *post-mortem* images of  $B_{xx}$  pillars shown in Fig. 3d, e, f, the images are sharpened for better visibility of slip traces. Non-sharpened images can be found in Fig. S2 in the supplementary document. As the contrast between the grains is lost after deformation, the position and shape of the GB cannot be exactly confirmed after the deformation across the GB length. In addition, the slip traces are not distinctly connected at the boundary, as would be the case for ideal slip transmission. The connected slip traces was previously shown for instance in the case of pillars with a CTB [12].

The stress–strain curve for each pillar was determined from load–displacement data based on the micropillar dimensions determined by SEM imaging. Fig. 4 shows the representative stress–strain curves of  $S_{xx}$  and  $B_{xx}$  pillars of two different sizes. At around each 5% strain, there is an intentional unloading step to zero stress to lower the lateral friction between the tip and the pillar top surface. The results indicate that the smaller pillars, with a diameter of 1.5  $\mu\text{m}$ , exhibit greater strength than the larger pillars. This observation is consistent with the well-known size effect observed in micropillars [45,46]. At a size of 3  $\mu\text{m}$ , the flow stress of  $S_{xx}$  and  $B_{xx}$  are comparable, whereas, at 1.5  $\mu\text{m}$ , the difference between them is slightly more pronounced. In addition, in the case of 3  $\mu\text{m}$  pillars, load drops are smaller than for 1.5  $\mu\text{m}$  pillars.

Fig. 5 shows the shear stress at 2% strains vs. pillar diameter for all compressed pillars. A size effect, as it is typically observed in micropillar compression testing is evident: pillars with smaller diameters tend to be stronger. In addition, more scattering could be seen at 1.5  $\mu\text{m}$  diameter, which can be explained by the scarcity of available dislocation sources in the confined body of the pillar [45,46]. The average values of normal stress for  $S_{xx}$  and  $B_{xx}$  pillars in two nominal sizes is provided in Table 1, assuming that slight differences in the nominal diameters do not

influence the pillar strength. According to this table, the shear stress difference ( $\Delta\tau_{2\%}$ ) between  $S_{xx}$  and  $B_{xx}$  for 3  $\mu\text{m}$  pillars is  $\Delta\tau_{2\%, 3 \mu\text{m}} \approx 2.7$  MPa, while it is slightly larger for 1.5  $\mu\text{m}$  pillars  $\Delta\tau_{2\%, 1.5 \mu\text{m}} \approx 5.7$  MPa. The shear stress is calculated from the normal stress using the highest Schmid factor (0.26) for each grain.

### 3.3. Compression of ITB pillars in the thickness of the film in $[1\bar{3}4]$ direction

The pillars in the [111] direction had multiple slip systems activated. Therefore, the dislocation–dislocation phenomena could partially mask the dislocation–ITB interaction. To investigate the transmission behaviour across ITBs, the second set of pillars was milled from the side of the film (as shown in Fig. 1b), oriented nominally in the  $[1\bar{3}4]$  compression direction. In this configuration, one system has the highest Schmid factor. The experimental procedure for milling these pillars is explained in section 2.2.

The *pre-* and *post-mortem* image of a single crystalline pillar in  $[1\bar{3}4]$  are shown in Fig. 6a and 6c, respectively. Fig. 6c shows that the deformation in  $S_{xx}$  pillar is concentrated at the top of the pillar, in a few but distinct slip steps. Up to around 8% strain, only one slip system with the highest Schmid factor is activated.

In the case of  $B_{xx}$  pillars in Fig. 6b, the ITB is in the center of the pillar on the top surface, but eventually exits at approximately middle of the pillar height. It is notable that in this compression direction, the GB plane is not perpendicular to the compression direction (see the schematic in Fig. 1c) and therefore does not run through the pillar vertically from top to bottom. The slip traces in  $B_{xx}$  pillars are more homogeneously spread in the pillar. Some less frequent secondary slip traces also can be found in the left grain. After deformation, no connected slip traces at the boundary can be found. The *post-mortem* images are sharpened for better detection of slip planes. The raw images can be found in Fig. S4 in the supplementary document.

Comparing the stress–strain curves of  $S_{xx}$  and  $B_{xx}$  in Fig. 6f shows that the flow stress of the  $B_{xx}$  pillar is  $\sim 50$  MPa larger than for the  $S_{xx}$ . There are numerous displacement bursts in the  $S_{xx}$  pillars, which –

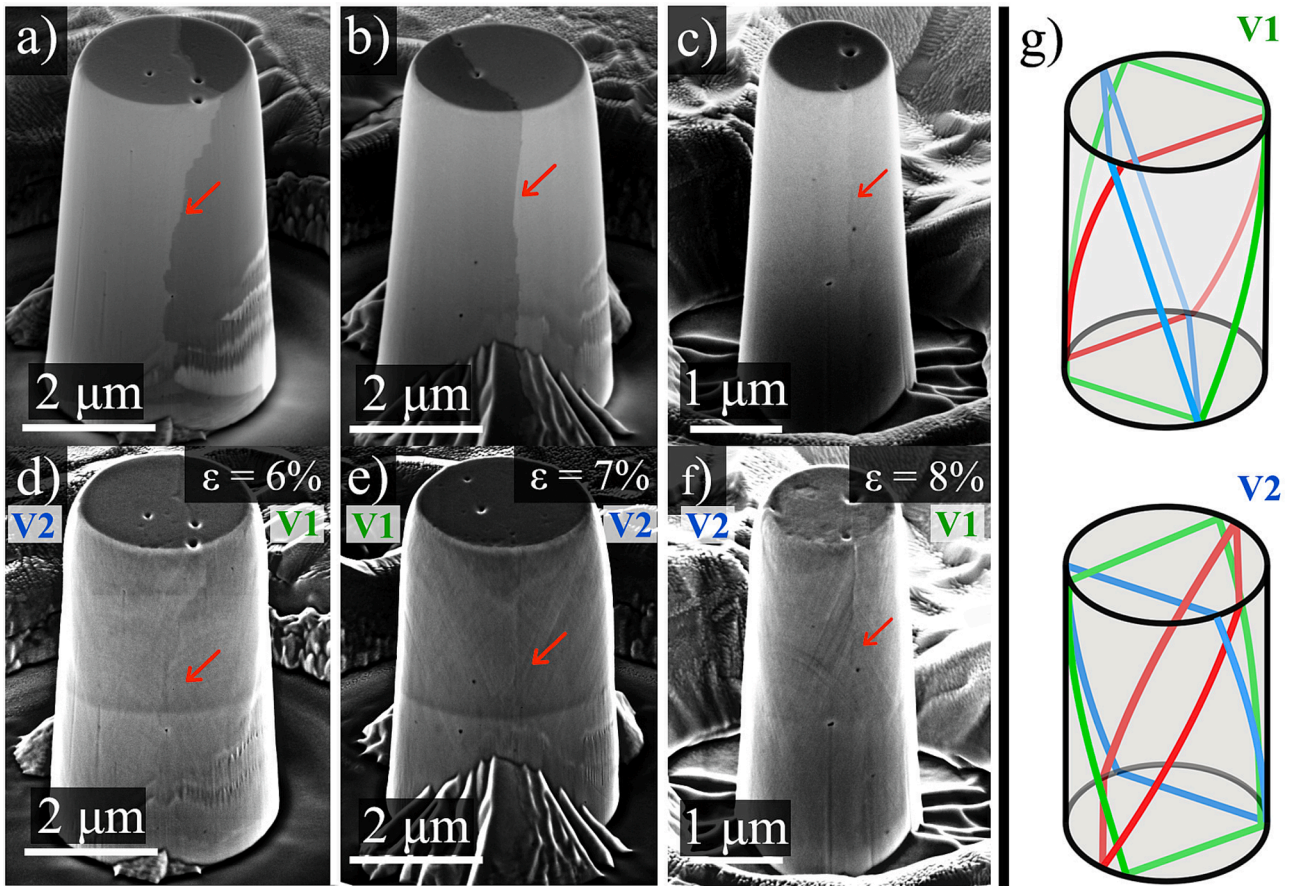


Fig. 3. a), b) and c) show the *pre-* and d), e) and f) the *post-mortem* SEM micrographs of Bxx pillars containing an ITB along [111] direction. The first two pillars are nominally 3 μm in diameter and the third 1.5 μm. The grain boundaries are marked with red arrows. There is a distinct channeling contrast between the two grains before deformation, which is lost after deformation. Because multiple slip systems are activated, the slip traces are in different directions and are faint. Note that the post mortem images are sharpened for better visibility of slip planes. g) shows schematics of all the 3 slip planes in each type of grain variant, that have 6 slip systems with the highest Schmid factor. (For interpretation of the references to colour in this figure legend, the reader is referred to the web version of this article.)

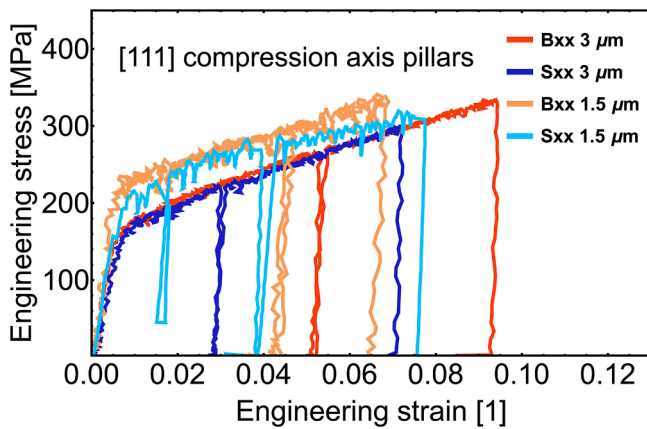


Fig. 4. Representative stress–strain curves of the single and bi-crystalline pillars in two sizes, in [111] compression direction. In the case of 3 μm pillars, the Sxx and Bxx curves are close to each other, while at 1.5 μm, Bxx pillars have higher flow stress than Sxx. The load drops in flow stress in smaller pillars are larger compared to 3 μm pillars. It should be noted that load drops to zero are intentional unloading steps.

together with the pseudo displacement control of the indenter – results in an unintentional unloading to zero force. On the contrary, other than the intentional unloading step, Bxx shows smaller load drops. Moreover, Sxx shows no sign of apparent strain hardening, while small apparent

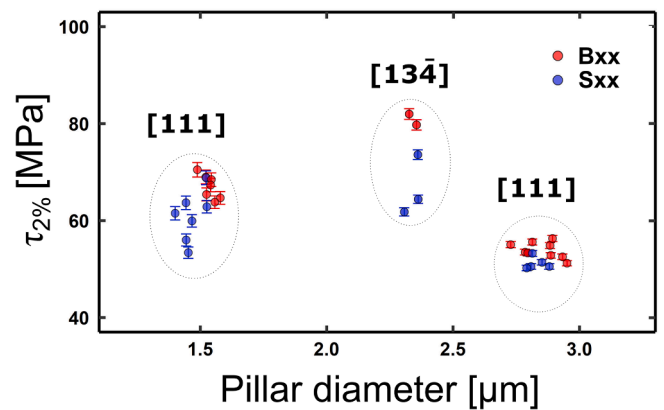


Fig. 5. The shear stress vs. pillar diameter of pillars compressed in [111] and [134] directions. The standard error bars of each experiment is shown for each symbol. Considering [111] direction, a size-effect is evident: smaller pillars are stronger. At a nominal size of 3 μm, the Bxx pillars are slightly stronger than the Sxx. The difference at 1.5 μm is more distinct and the Bxx pillars are ~ 5.7 MPa stronger than their Sxx pillar counterparts are. Pillars in [134] direction are milled in one diameter and two Bxx pillars are stronger than Sxx in this direction.

**Table 1**

The average value of normal stress for Sxx and Bxx pillars in [111] direction in two nominal sizes of 1.5 and 3 μm. The diameter is measured at the top and bottom of the pillar and the average value is reported.

Pillar type	Nominal pillar diameter (μm)	Measured average diameter (μm)	σ <sub>2%</sub> average (MPa)
Sxx	1.5	1.48 ± 0.04	236.3 ± 6.8
Bxx	1.5	1.54 ± 0.03	258.8 ± 3.5
Sxx	3	2.82 ± 0.03	196.9 ± 2.1
Bxx	3	2.85 ± 0.02	207.4 ± 2.1

hardening is observed in the case of the Bxx pillar(s).

In total, 5 annular pillars were successfully tested in [134] compression direction. As the compression direction is slightly different (~5°) in the two Bxx grains (see IPF in Fig. 6e), the average of the

highest Schmid factor of each grain ( $m_1 = 0.44$  and  $m_2 = 0.46$ ) has been used to calculate the shear stress ( $\tau_{2\%}$ ) of Bxx. The shear stress vs diameter of all pillars in [134] and [111] directions is shown in Fig. 5. A shear stress difference  $\Delta\tau_{2\%} \approx 17.5$  MPa between Sxx and Bxx pillars is observed for [134] pillars.

One aspect of ideal slip transmission across a CTB was the distinct slip traces connected at the boundary [12,14,15]. Indications of connected slip traces could be not found in the annular pillars in [134] direction. Aiming for a better observation of the boundary with SEM and EBSD, some annular pillars were cut in the middle prior to pillar compression to have a flat surface as shown in Fig. 7a. However, as evident in Fig. 7a and 7b, curtaining prevented the surface from being entirely smooth, which therefore obscured the observation of small features in the *post-mortem* analysis. This was likely caused by the previous milling step, where the excess part of the freestanding film was

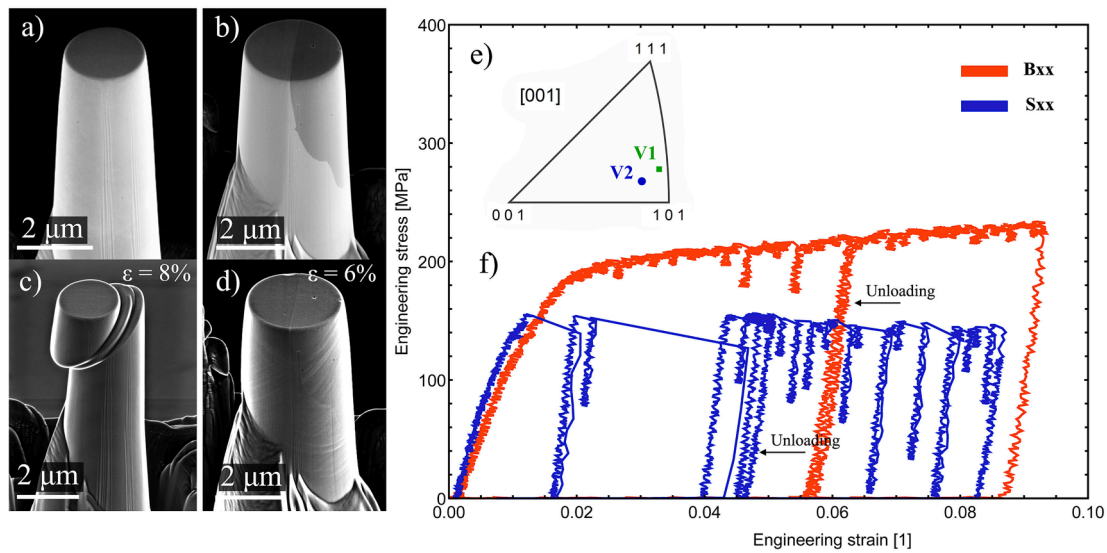


**Fig. 6.** Pre- and post-mortem SEM micrographs of a Sxx a) and c), and Bxx pillar b) and d) in [134] direction. The post-mortem images are sharpened for better visibility of slip traces. e) Inverse pole figure of the compression direction of the two grains. f) shows the stress–strain curve of the Sxx and Bxx. The Bxx deforms at higher stresses and shows fewer load drops. Arrows mark the intentional unloading steps.

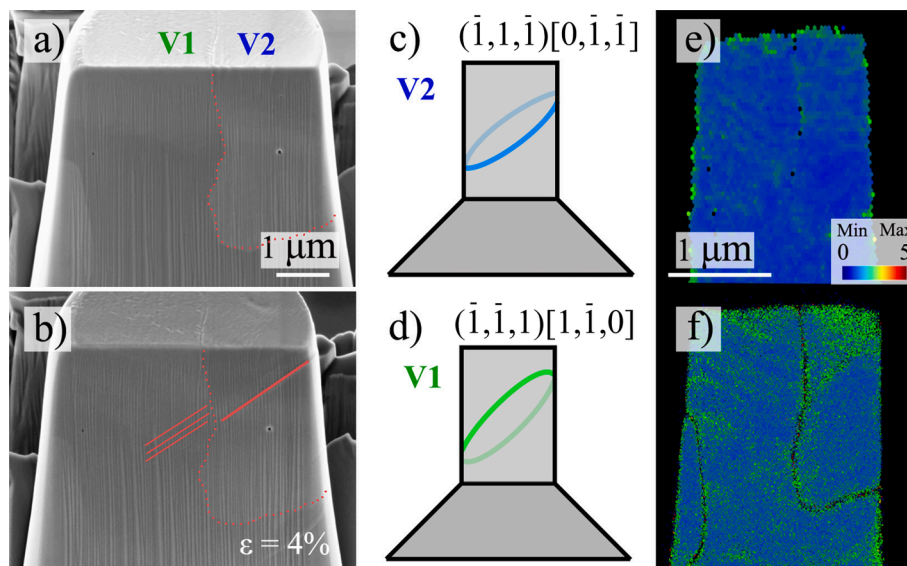


**Fig. 7.** Before and after deformation of a pillar with a flat side containing incoherent boundaries. a) and b) are pre- and post-mortem SEM images, c) and d) schematically show the slip system with the highest Schmid factor in each grain. c) The activated glide system  $(\bar{1}, 1, \bar{1})[0, \bar{1}, \bar{1}]$  in grain V2 has a Schmid factor of 0.44 and d) 0.46 for grain V1 with the glide system  $(\bar{1}, \bar{1}, 1)[1, \bar{1}, 0]$ . e) and f) are KAM maps before and after deformation calculated from EBSD data.

removed with FIB. This step may have introduced some surface unevenness, leading to curtaining. The curtaining existed even in surfaces that were milled with FIB currents as low as 10 pA. The *post-mortem* image of this pillar is shown in Fig. 7b. A distinct slip trace in the right grain close to the top surface is visible. The continuation of this slip with the highest Schmid factor in the left grain (red lines) is, however, multifold and more faint, and seems to deviate from the incoming slip plane from the right grain.

Having a flat surface is also beneficiary in taking EBSD before and after deformation. Fig. 7e and 7f show kernel average (KAM) misorientation maps of the pillar before and after deformation, respectively. Notably, a low misorientation ( $<3^\circ$ ) is observed in the pillar before deformation. This confirms that the freestanding film after preparation and sapphire fracture does not have a considerable density of stored dislocations. The *post-mortem* KAM also shows small misorientation ( $<3^\circ$ ) at the boundary, indicating that the boundary does not entirely block the dislocation transmission which would lead to pile ups. We interpret the weak decoration of the ITB with geometrically necessary dislocations (GND) and the spread of incoming slip traces in several slip traces (Fig. 7) as indications for slip transmission. The primary slip planes with the highest Schmid factor are marked in Fig. 7c and d. Keeping the Thompson tetrahedral of two grains in Fig. 1c in mind, the slip systems of the two grains do not facilitate an easy transmission based on the slip geometry. As no common plane or direction can be found between the systems, complex behavior of dislocation at the boundary is required for slip transmission.

## 4. Discussion

### 4.1. Remarks of milling pillars with an ITB on a Cu film

Fabrication of bulk samples with a defined GB for micro-compression tests can be done using various methods such as the Bridgeman technique or diffusion bonding [47]. The advantage of a bulk bi-crystalline sample is that a slice of a macro sample can be used to mill numerous pillars with the exact same grain boundary. This is beneficial in achieving the statistics that is usually required to quantify the mechanisms of slip transmission in micron-sized samples.

In the case of ITBs, thin film deposition was chosen to synthesize the Cu sample. As the GB energy of the boundary is more than one order of magnitude higher than for the CTB (see the Introduction), bi-crystal growth with the Bridgeman technique (which was previously used for Bxx growth of CTB [12,15]) was not employed, because the GB was expected to deviate to other lower energy boundary planes. Using the film sputtering method, one can use the orientation relationships of the crystal to the substrate to motivate the growth of certain crystal orientations and, thus, specific GBs [27]. Besides being able to produce specific GBs, milling pillars on a thin film on a sapphire substrate, compared to a bulk sample, also provides a rigid base for the pillars. Plastic material sink-in and the movement of the dislocation into the base of the pillars [44] are thus suppressed by the sapphire substrate.

Hieke et al. [27] showed that depositing Al on single crystalline sapphire,  $\Sigma 3\{112\}$  ITBs are present between two grains variants in orientation relationships OR I. Also Bishara et al. [41] revealed that a Cu film with  $\sim 490$  nm thickness on sapphire contains straight  $\Sigma 3\{112\}$  ITBs that extend from the surface to the substrate. The sputtered Cu film in this work also possessed two variants with  $[111]$  normal direction that had  $\Sigma 3\{112\}$  ITBs between them. However, the minimum thickness required for micropillar milling must be taken into account. In this case, where pillars of up to  $3\ \mu\text{m}$  in diameter were aimed, a film thickness of at least  $6\ \mu\text{m}$  was necessary so that the diameter to height ratio of  $\sim 2$  could be maintained. In the  $6\ \mu\text{m}$  thick film, boundaries were not always straight and large or small CTB facets could be found at the ITB boundary. Therefore, some pillars could only be classified as bi-crystalline after *post-mortem* FIB milling. Moreover, CTB sections needed to be taken into account when discussing the strength

contribution of tested boundaries to the overall pillar strength.

While compressing the pillars in  $[111]$  direction activated multiple slips, another compression direction was needed, where fewer systems (ideally one) are activated. This enables us to focus on the interaction between GBs and dislocations, rather than on dislocation–dislocation interactions. Since the film is thin in one dimension ( $6\ \mu\text{m}$ ), the compression axis of the second set of pillars could only be selected normal to the film surface, as depicted in Fig. 1b. Handling the substrate in this configuration was challenging, because the sapphire substrate could not be easily removed. In the case of other substrates, either etching (for silicon [47,48]) or dissolving (for NaCl [49]) could remove the substrate and leave an entirely detached and freestanding film. The fact that we used a partially freestanding film (see Fig. 1b) required long FIB cuts to remove the redundant part of the film. This and needing to mill pillars on the edge of the film meant that only a limited number of pillars in this configuration could be milled and tested. Nevertheless, this configuration allowed testing pillars containing ITBs with single slip activation.

### 4.2. Can dislocations transmit through ITBs?

In bi-crystalline pillars, the incompatibility stresses due to different grain orientations and elastic and plastic anisotropy may change the stress state in the pillar [50], causing the activation of other slip systems than predicted by Schmid's law. In the  $[111]$  pillars of this study, the compression direction is the same in both grains and therefore no anisotropy is expected. For  $[13\bar{4}]$  pillars, the slip traces after deformation agree with those predicted by Schmid's law. Therefore, we conclude that activation of dislocation sources are on planes with the nominally highest shear stress as predicted by Schmid's law, and not caused by compatibility stress.

To answer whether dislocations can transmit through ITBs or not, the meeting point of slip traces at the boundary can be analysed. In the case of easy transmission, distinct slip traces are connected at the boundary, like in ideal slip transmission across a CTB [12,15]. In  $[111]$  pillars, multi-slip activation caused faint slip traces both in Sxx and Bxx. Therefore,  $[111]$  compression direction at the micron scale is not suitable for observing slip transmission. In the case of  $[13\bar{4}]$  pillars, where mostly one slip system in each grain is activated, slip traces are not distinctly connected at the boundary. For instance, Fig. 7b shows that the distinct slip in the right grain is continued by numerous faint and less distinct slip traces in the left grain. Besides, *post mortem* KAM reveals no sign of GNDs storage at the GB, indicating that dislocations can penetrate the boundary. The small apparent strain hardening in  $[13\bar{4}]$  Bxx pillars in Fig. 6 also suggests that the boundary is penetrable. Therefore, it can be inferred that the dislocations can transmit across ITB, although transmission on a pre-defined path does not take place.

Shear stress difference ( $\Delta\tau_{2\%}$ ) between Sxx and Bxx pillars can also be utilized to determine whether slip transmission occurs or not. If the GB is impenetrable, the Bxx pillars can be considered as two separate pillars that are attached to each other. It is well-established that size-scaling has an impact on the strength of pillars, with smaller pillars exhibiting greater strength. Therefore, the strength of Bxx pillars with an impenetrable boundary would scale with half of the pillar diameter ( $d/2$ ), which represents the effective dislocation size [51]. In our previous work [12], a power-law relation was derived to predict the strength of Cu pillars in different sizes, based on the approach of Dou and Derby [52]. Using the power law for pillars in  $[13\bar{4}]$  direction, with  $d = 2.4\ \mu\text{m}$  (corresponding to Sxx) and  $d = 1.2\ \mu\text{m}$  (corresponding to a Bxx pillar with an impenetrable boundary),  $\Delta\tau_{2\%}$  is expected to be  $\sim 35$  MPa. The estimated  $\Delta\tau_{2\%}$  is larger than what we measured (17.5 MPa) for  $[13\bar{4}]$ , which again suggests that the ITB is penetrable. One example of compression of a bi-crystalline pillar with an impenetrable boundary can be found in the work of Imrich et al. [13]. In that case, a large apparent strain hardening was observed and bi-crystalline pillars were 19–41%

stronger than the Sxx ones. It is important to note that despite indications of slip transmission, the measurement of slip transmission is not feasible.

Fig. 5 shows the shear stress ( $\tau_{2\%}$ ) vs. the pillar diameter for both compression directions of [1 1 1] and [13  $\bar{4}$ ]. It is interesting that pillars in [13  $\bar{4}$ ] direction deform at higher shear stresses compared to [1 1 1] pillars. This difference might have two explanations: i) Because 6 slip systems are activated in [1 1 1] compression direction, there is a higher chance that a dislocation source with lower activation energy (stress) is present in the body of the pillar. ii) pillars are milled and compressed at two different conditions. The difference in alignment, tearing of the Cu film prior to obtaining a freestanding film portion, and more extensive FIB milling for [13  $\bar{4}$ ] pillars could cause more damage [53] and thus higher flow stress.

The discussion on the transmission of dislocations has thus far been based on the assumption that the ITB has a GB plane of {1 1 2}. However, it is important to note that numerous large and small steps of CTB can be observed along the boundary. Therefore, the experiments measured the collective behavior of such boundaries. Different mechanisms could be considered to explain the present, but not large  $\Delta\tau_{2\%}$  in case of ITB pillars:

a) Transmission of dislocations through CTB steps could be considered. In our previous work [12], pillars with a CTB in different sizes were tested. The strength increases in pillars containing a CTB was explained by the dislocation curvature penalty needed for reorientation of the dislocation, so that they have a screw character and can cross-slip to the next grain. A probability function was derived to predict the strength increase caused by the presence of a CTB in different pillar sizes [12]. According to this probability function, there is a 50% probability that pillars with a CTB at 2.4  $\mu\text{m}$  diameter are 7 MPa stronger than their Sxx counterparts. This is indeed lower than what we measured for  $\Delta\tau_{2\%} \approx 17.5$  MPa in the case of ITB pillars compressed at [13  $\bar{4}$ ]. The difference in  $\Delta\tau_{2\%}$  values indicates that CTB segments alone cannot explain the transmission behavior.

b) The indirect transmission through the {1 1 2} ITB is another possibility. As discussed in section 3.3, the two slip systems with the highest Schmid factor do not have a common plane or direction for easy transmission. This is also confirmed by the transmission factor  $m'$  based on the Luster and Morris criterion [54], which is between 0 (no transmission) and 1 (perfect alignment for dislocation transmission). This was calculated to be  $m' = 0.4$  for the pillar in [13  $\bar{4}$ ] compression direction. As the alignment is not ideal for easy slip transmission, non-conservative motion and/or reactions with the partial dislocations forming the ITB and/or possible GB dislocations (disconnections), followed by subsequent emission to the next grain is required. As shown in Fig. 7b, the incoming distinct slip trace from the right grain is continued by numerous faint and parallel slip traces in the adjacent grain. This can be an indication of an indirect slip transmission. Moreover, Ma et al. [38] in a simulation study showed that the transmission behavior of dislocation through ITB is dependent on where the gliding dislocation meets one of the three pre-existing partial dislocations, which are present at ITBs. Such interactions cannot be observed in a micron-sized sample. However, the fact that some slip traces exit the boundary in different planes compared to the incoming plane, shows that parts of the boundary are more favorable for transmission or for emission of dislocations to the second grain. Therefore, alignment of the dislocation Burgers vectors, their movement on the GB plane, and their reaction with the ITB partials can explain the strength increase of Bxx pillars.

## 5. Summary and conclusions

Micropillar compression of pillars containing an ITB showed that dislocations can transmit through ITB, and the strength of the Bxx pillars is increased ( $\Delta\tau_{2\%}$ ) compared to Sxx pillars. The magnitude of  $\Delta\tau_{2\%}$  depends on the pillar size, as well as the compression direction of the

grains. It has been previously shown that in dislocation transmission through CTB, additional curvature of the dislocation is responsible for the size-dependent stress increase of pillars. In pillars containing ITB, however, ideal slip transmission does not likely take place and the dislocation transmission is more complicated. This can be confirmed by *post-mortem* images of the pillars in [13 $\bar{4}$ ] directions: the slip traces are not distinctly connected at the boundary. Comparing the two slip directions, only the [13 $\bar{4}$ ] direction allows for observing signs of slip transmission as multiple slip in the [111] case prevents the observation of slip traces.

The testing of high energy ITBs at the micron-scale involved utilizing the geometrical relationship between the film and the substrate (sapphire in this case). ITBs that were grown in the film had several long and short CTB steps in them, which is expected at this length scale due their large energy differences. The result of this work can be used in studying complex systems to predict the mechanical response, where ITBs are frequent or present alongside CTBs.

## Declaration of Competing Interest

The authors declare that they have no known competing financial interests or personal relationships that could have appeared to influence the work reported in this paper.

## Data availability

Data will be made available on request.

## Acknowledgements

The authors gratefully thank Dr. Hanna Bishara for helping in the thin film deposition and Leon Christiansen for assistance in pillar milling. GD acknowledges the European Research Council for funding part of this project (Grant no. 787446-GB-CORRELATE). Financial support by the Robert Bosch Foundation is gratefully acknowledged by CK.

## Declaration of Generative AI and AI-assisted technologies in the writing process

During the preparation of this work, the authors used ChatGPT in order to improve the readability of parts of the text. After using this tool/service, the authors reviewed and edited the content as needed and take (s) full responsibility for the content of the publication.

## Appendix A. Supplementary data

Supplementary data to this article can be found online at <https://doi.org/10.1016/j.matdes.2023.112164>.

## References

- [1] T. Nguyen, D.J. Luscher, J.W. Wilkerson, A dislocation-based crystal plasticity framework for dynamic ductile failure of single crystals, *J. Mech. Phys. Solids*. 108 (2017) 1–29, <https://doi.org/10.1016/j.jmps.2017.07.020>.
- [2] T.R. Bieler, P. Eisenlohr, F. Roters, D. Kumar, D.E. Mason, M.A. Crimp, D. Raabe, The role of heterogeneous deformation on damage nucleation at grain boundaries in single phase metals, *Int. J. Plast.* 25 (2009) 1655–1683, <https://doi.org/10.1016/j.ijplas.2008.09.002>.
- [3] L. Rémy, Interaction between slip and twinning systems and the influence of twinning on the mechanical behavior of fcc metals and alloys, in: *Metall. Trans. A, Phys. Metall. Mater. Sci.* 12, A, 1981, pp. 387–408, <https://doi.org/10.1007/BF02648536>.
- [4] Y.T. Zhu, X.Z. Liao, X.L. Wu, Deformation twinning in nanocrystalline materials, *Prog. Mater. Sci.* 57 (2012) 1–62, <https://doi.org/10.1016/j.pmatsci.2011.05.001>.
- [5] J. Wang, N. Li, A. Misra, Structure and stability of  $\Sigma 3$  grain boundaries in face centered cubic metals, *Philos. Mag.* 93 (2013) 315–327, <https://doi.org/10.1080/14786435.2012.716908>.
- [6] N. Bernstein, E.B. Tadmor, Tight-binding calculations of stacking energies and twinnability in fcc metals, *Phys. Rev. B - Condens. Matter Mater. Phys.* 69 (2004) 1–10, <https://doi.org/10.1103/PhysRevB.69.094116>.



- [7] D.M. Saylor, B.S. El Dasher, A.D. Rollett, G.S. Rohrer, Distribution of grain boundaries in aluminum as a function of five macroscopic parameters, *Acta Mater.* 52 (2004) 3649–3655, <https://doi.org/10.1016/j.actamat.2004.04.018>.
- [8] M. Dao, L. Lu, Y.F. Shen, S. Suresh, Strength, strain-rate sensitivity and ductility of copper with nanoscale twins, *Acta Mater.* 54 (2006) 5421–5432, <https://doi.org/10.1016/j.actamat.2006.06.062>.
- [9] L. Lu, X. Chen, X. Huang, K. Lu, Revealing the maximum strength in nanotwinned copper, *Science* 323 (2009) 607–610, <https://doi.org/10.1126/science.1167641>.
- [10] L. Lu, Y. Shen, X. Chen, L. Qian, K. Lu, Ultrahigh Strength and High Electrical Conductivity in Copper, *Science* 304 (2004) 422–426, <https://doi.org/10.1126/science.1092905>.
- [11] K. Lu, L. Lu, S. Suresh, Strengthening materials by engineering coherent internal boundaries at the nanoscale, *Science* 324 (2009) 349–352, <https://doi.org/10.1126/science.1159610>.
- [12] R. Hosseinabadi, H. Riesch-Oppermann, J.P. Best, G. Dehm, C. Kirchlechner, Size scaling in bi-crystalline Cu micropillars containing a coherent twin boundary, *Acta Mater.* 230 (2022), 117841, <https://doi.org/10.1016/j.actamat.2022.117841>.
- [13] P.J. Imrich, C. Kirchlechner, C. Motz, G. Dehm, Differences in deformation behavior of bicrystalline Cu micropillars containing a twin boundary or a large-angle grain boundary, *Acta Mater.* 73 (2014) 240–250, <https://doi.org/10.1016/j.actamat.2014.04.022>.
- [14] N.V. Malyar, J.S. Micha, G. Dehm, C. Kirchlechner, Dislocation-twin boundary interaction in small scale Cu bi-crystals loaded in different crystallographic directions, *Acta Mater.* 129 (2017) 91–97, <https://doi.org/10.1016/j.actamat.2017.02.067>.
- [15] N.V. Malyar, B. Grabowski, G. Dehm, C. Kirchlechner, Dislocation slip transmission through a coherent  $\Sigma\{111\}$  copper twin boundary: Strain rate sensitivity, activation volume and strength distribution function, *Acta Mater.* 161 (2018) 412–419, <https://doi.org/10.1016/j.actamat.2018.09.045>.
- [16] J.P. Liebig, S. Krauß, M. Göken, B. Merle, Influence of stacking fault energy and dislocation character on slip transfer at coherent twin boundaries studied by micropillar compression, *Acta Mater.* 154 (2018) 261–272, <https://doi.org/10.1016/j.actamat.2018.05.037>.
- [17] V. Samaee, M. Dupraz, T. Pardoen, H. Van Swygenhoven, D. Schryvers, H. Idrissi, Deciphering the interactions between single arm dislocation sources and coherent twin boundary in nickel bi-crystal, *Nat. Commun.* 12 (2021) 962, <https://doi.org/10.1038/s41467-021-21296-z>.
- [18] L.L. Li, X.H. An, P.J. Imrich, P. Zhang, Z.J. Zhang, G. Dehm, Z.F. Zhang, Microcompression and cyclic deformation behaviors of coaxial copper bicrystals with a single twin boundary, *Scr. Mater.* 69 (2013) 199–202, <https://doi.org/10.1016/j.scriptamat.2013.04.004>.
- [19] M. Chassigne, M. Legros, D. Rodney, Atomic-scale simulation of screw dislocation/coherent twin boundary interaction in Al, Au, Cu and Ni, *Acta Mater.* 59 (2011) 1456–1463, <https://doi.org/10.1016/j.actamat.2010.11.007>.
- [20] Z.H. Jin, P. Gumbsch, K. Albe, E. Ma, K. Lu, H. Gleiter, H. Hahn, Interactions between non-screw lattice dislocations and coherent twin boundaries in face-centered cubic metals, *Acta Mater.* 56 (2008) 1126–1135, <https://doi.org/10.1016/j.actamat.2007.11.020>.
- [21] M. Dupraz, S.I. Rao, H. Van Swygenhoven, Large scale 3-dimensional atomistic simulations of screw dislocations interacting with coherent twin boundaries in Al, Cu and Ni under uniaxial and multiaxial loading conditions, *Acta Mater.* 174 (2019) 16–28, <https://doi.org/10.1016/j.actamat.2019.05.025>.
- [22] Y.M. Wang, F. Sansoz, T. LaGrange, R.T. Ott, J. Marian, T.W. Barbee, A.V. Hamza, Defective twin boundaries in nanotwinned metals, *Nat. Mater.* 12 (8) (2013) 697–702, <https://doi.org/10.1038/nmat3646>.
- [23] C. Schmidt, M.W. Finnis, F. Ernst, V. Vitek, Theoretical and experimental investigations of structures and energies of  $\Sigma = 3$ , [112] tilt grain boundaries in copper, *Philos. Mag. A Phys. Condens. Matter, Struct. Defects Mech. Prop.* 77 (1998) 1161–1184, <https://doi.org/10.1080/01418619808214246>.
- [24] U. Wolf, F. Ernst, T. Muschik, M.W. Finnis, H.F. Fischmeister, The influence of grain boundary inclination on the structure and energy of  $\sigma = 3$  grain boundaries in copper, *Philos. Mag. A Phys. Condens. Matter, Struct. Defects Mech. Prop.* 66 (1992) 991–1016, <https://doi.org/10.1080/01418619208248003>.
- [25] E.R. Homer, S.M. Foiles, E.A. Holm, D.L. Olmsted, Phenomenology of shear-coupled grain boundary motion in symmetric tilt and general grain boundaries, *Acta Mater.* 61 (2013) 1048–1060, <https://doi.org/10.1016/j.actamat.2012.10.005>.
- [26] G. Dehm, M. Rühle, G. Ding, R. Raj, Growth and structure of copper thin films deposited on (0001) sapphire by molecular beam epitaxy, *Philos. Mag. B Phys. Condens. Matter; Stat. Mech. Electron. Opt. Magn. Prop.* 71 (1995) 1111–1124, <https://doi.org/10.1080/01418639508241899>.
- [27] S.W. Hieke, B. Breitbach, G. Dehm, C. Scheu, Microstructural evolution and solid state dewetting of epitaxial Al thin films on sapphire ( $\alpha$ -Al<sub>2</sub>O<sub>3</sub>), *Acta Mater.* 133 (2017) 356–366, <https://doi.org/10.1016/j.actamat.2017.05.026>.
- [28] S.W. Hieke, M.G. Willinger, Z.J. Wang, G. Richter, D. Chatain, G. Dehm, C. Scheu, On pinning-depinning and microkink-flow in solid state dewetting: Insights by in-situ ESEM on Al thin films, *Acta Mater.* 165 (2019) 153–163, <https://doi.org/10.1016/j.actamat.2018.11.028>.
- [29] G. Dehm, H. Edougué, T. Wagner, S.H. Oh, E. Arzt, Obtaining different orientation relationships for Cu films grown on (0001)  $\alpha$ -Al<sub>2</sub>O<sub>3</sub> substrates by magnetron sputtering, *Int. J. Mater. Res.* 96 (2005) 249–254, <https://doi.org/10.3139/jmr-2005-0045>.
- [30] G. Dehm, B.J. Inkson, T. Wagner, Growth and microstructural stability of epitaxial Al films on (0001)  $\alpha$ -Al<sub>2</sub>O<sub>3</sub> substrates, *Acta Mater.* 50 (2002) 5021–5032, [https://doi.org/10.1016/S1359-6454\(02\)00347-6](https://doi.org/10.1016/S1359-6454(02)00347-6).
- [31] D. Amram, L. Klinger, N. Gazit, H. Gluska, E. Rabkin, Grain boundary grooving in thin films revisited: The role of interface diffusion, *Acta Mater.* 69 (2014) 386–396, <https://doi.org/10.1016/j.actamat.2014.02.008>.
- [32] Y. Addab, M.K. Kini, B. Courtois, A. Savan, A. Ludwig, N. Bozzolo, C. Scheu, G. Dehm, D. Chatain, Microstructure evolution and thermal stability of equiatomic CoCrFeNi films on (0001)  $\alpha$ -Al<sub>2</sub>O<sub>3</sub>, *Acta Mater.* 200 (2020) 908–921, <https://doi.org/10.1016/j.actamat.2020.09.064>.
- [33] J. Wang, O. Anderoglu, J.P. Hirth, A. Misra, X. Zhang, Dislocation structures of  $\sigma_3$  {112} twin boundaries in face centered cubic metals, *Appl. Phys. Lett.* 95 (2009) 1–4, <https://doi.org/10.1063/1.3176979>.
- [34] N. Lu, K. Du, L. Lu, H.Q. Ye, Motion of 1/3{111} dislocations on  $\Sigma$  {112} twin boundaries in nanotwinned copper, *J. Appl. Phys.* 115 (2014), <https://doi.org/10.1063/1.4861868>.
- [35] J. Wang, N. Li, O. Anderoglu, X. Zhang, A. Misra, J.Y. Huang, J.P. Hirth, Detwinning mechanisms for growth twins in face-centered cubic metals, *Acta Mater.* 58 (2010) 2262–2270, <https://doi.org/10.1016/j.actamat.2009.12.013>.
- [36] N. Li, J. Wang, J.Y. Huang, A. Misra, X. Zhang, Influence of slip transmission on the migration of incoherent twin boundaries in epitaxial nanotwinned Cu, *Scr. Mater.* 64 (2011) 149–152, <https://doi.org/10.1016/j.scriptamat.2010.09.031>.
- [37] Y. Liang, X. Yang, M. Gong, G. Liu, Q. Liu, J. Wang, Slip transmission for dislocations across incoherent twin boundary, *Scr. Mater.* 166 (2019) 39–43, <https://doi.org/10.1016/j.scriptamat.2019.02.042>.
- [38] T. Ma, H. Kim, N. Mathew, D.J. Luscher, L. Cao, A. Hunter, Dislocation transmission across  $\Sigma$ 3{112} incoherent twin boundary: a combined atomistic and phase-field study, *Acta Mater.* 223 (2022), 117447, <https://doi.org/10.1016/j.actamat.2021.117447>.
- [39] M.D. Uchic, D.M. Dimiduk, J.N. Florando, W.D. Nix, Sample dimensions influence strength and crystal plasticity, *Science* 305 (2004) 986–989, <https://doi.org/10.1126/science.1098993>.
- [40] T.A. Parthasarathy, S.I. Rao, D.M. Dimiduk, M.D. Uchic, D.R. Trinkle, Contribution to size effect of yield strength from the stochastics of dislocation source lengths in finite samples, *Scr. Mater.* 56 (2007) 313–316, <https://doi.org/10.1016/j.scriptamat.2006.09.016>.
- [41] H. Bishara, M. Ghidelli, G. Dehm, Approaches to Measure the Resistivity of Grain Boundaries in Metals with High Sensitivity and Spatial Resolution: A Case Study Employing Cu, *ACS Appl. Electron. Mater.* 2 (2020) 2049–2056, <https://doi.org/10.1021/acsaem.0c00311>.
- [42] S. Huang, J. Lin, N. Wang, B. Guo, F. Jiang, Q. Wen, X. Lu, Fracture behavior of single-crystal sapphire in different crystal orientations, *Crystals* 11 (8) (2021) 930, <https://doi.org/10.3390/cryst11080930>.
- [43] C. Kirchlechner, J. Keckes, C. Motz, W. Grosinger, M.W. Kapp, J.S. Micha, O. Ulrich, G. Dehm, Impact of instrumental constraints and imperfections on the dislocation structure in micron-sized Cu compression pillars, *Acta Mater.* 59 (2011) 5618–5626, <https://doi.org/10.1016/j.actamat.2011.05.037>.
- [44] D. Kiener, C. Motz, G. Dehm, Micro-compression testing: A critical discussion of experimental constraints, *Mater. Sci. Eng. A* 505 (2009) 79–87, <https://doi.org/10.1016/j.msea.2009.01.005>.
- [45] J.R. Greer, J.T.M. De Hosson, Plasticity in small-sized metallic systems: Intrinsic versus extrinsic size effect, *Prog. Mater. Sci.* 56 (2011) 654–724, <https://doi.org/10.1016/j.pmatsci.2011.01.005>.
- [46] O. Kraft, P.A. Gruber, R. Mönig, D. Weygand, Plasticity in Confined Dimensions, *Annu. Rev. Mater. Res.* 40 (2010) 293–317, <https://doi.org/10.1146/annurev-matsci-082908-145409>.
- [47] N.V. Malyar, H. Springer, J. Wichert, G. Dehm, C. Kirchlechner, Synthesis and mechanical testing of grain boundaries at the micro and sub-micro scale, *Mater. Test.* 61 (2019) 5–18, <https://doi.org/10.3139/120.111286>.
- [48] M.K. Kini, G. Dehm, C. Kirchlechner, Size dependent strength, slip transfer and slip compatibility in nanotwinned silver, *Acta Mater.* 184 (2019) 120–131, <https://doi.org/10.1016/j.actamat.2019.11.042>.
- [49] G. Dehm, Miniaturized single-crystalline fcc metals deformed in tension: New insights in size-dependent plasticity, *Prog. Mater. Sci.* 54 (2009) 664–688, <https://doi.org/10.1016/j.pmatsci.2009.03.005>.
- [50] I. Tiba, T. Richeton, C. Motz, H. Vehoff, S. Berbenni, Incompatibility stresses at grain boundaries in Ni bicrystalline micropillars analyzed by an anisotropic model and slip activity, *Acta Mater.* 83 (2015) 227–238, <https://doi.org/10.1016/j.actamat.2014.09.033>.
- [51] C. Kirchlechner, Dislocation slip transfer mechanisms: quantitative insights from in situ micro-mechanical Testing, Habilitation Thesis, Montanuniversität Leoben (2017).
- [52] R. Dou, B. Derby, A universal scaling law for the strength of metal micropillars and nanowires, *Scr. Mater.* 61 (2009) 524–527, <https://doi.org/10.1016/j.scriptamat.2009.05.012>.
- [53] D. Kiener, C. Motz, M. Rester, M. Jenko, G. Dehm, FIB damage of Cu and possible consequences for miniaturized mechanical tests, *Mater. Sci. Eng. A* 459 (2007) 262–272, <https://doi.org/10.1016/j.msea.2007.01.046>.
- [54] E. Bayerschen, A.T. McBride, B.D. Reddy, T. Böhlke, Review on slip transmission criteria in experiments and crystal plasticity models, *J. Mater. Sci.* 51 (2016) 2243–2258, <https://doi.org/10.1007/s10853-015-9553-4>.